Sintering—Pressure- and Temperature-Dependent Contact Models

T. Weinhart, R. Fuchs, T. Staedler, M. Kappl and S. Luding

Introduction

Granular materials—conglomerates of discrete particles—are of paramount importance in the chemical, pharmaceutical, agri-food, energy, high-tech, materials, manufacturing, mining and construction industries. Handling and processing of particulates is a huge market, with annual revenues of €660 billion [8], making such particulate materials the most widely manipulated substance after water [5]. Here, we focus on sintering, i.e., the process of compacting and transforming a free-flowing particulate mass into a solid object by applying heat and/or pressure, without melting it completely. Additive manufacturing, tabletting, and moulding are just a few applications in which sintering plays a role.

To better understand the sintering of granular materials, we take a bottom-up approach: First, the particle and contact properties of the particles that constitute the granular material are measured experimentally. This data is then used to construct contact laws and particle properties, paying special attention to pressure- and temperature-dependence. Those laws are then applied to model the granular

T. Weinhart (✉) · S. Luding
University of Twente, Enschede, The Netherlands
e-mail: t.weinhart@utwente.nl

S. Luding
e-mail: s.luding@utwente.nl

R. Fuchs
Evonik Technology & Infrastructure GmbH, Hanau, Germany
e-mail: regina.fuchs@evonik.com

T. Staedler
Universität Siegen, Siegen, Germany
e-mail: staedler@lot.mb.uni-siegen.de

M. Kappl
MPI for Polymer Research, Mainz, Germany
e-mail: kappl@mpip-mainz.mpg.de

S. Antonyuk (ed.), *Particles in Contact*,
https://doi.org/10.1007/978-3-030-15899-6_10

materials via Discrete Particle Simulations, which explicitly follow the motion of each individual particle by applying forces and torques that stem either from external (body) forces or from interactions with other particles or walls. Those simulations, properly calibrated, can then be used to predict the qualities of a sintered product (e.g., its tensile strength, elasticity, or brittleness) including the whole process chain: the cold, lose powder, the sintering process by increased pressure and heat, the cool-down, and the final testing phases.

This chapter summarises the advances made in modelling pressure-, temperature-, and time-dependent granular processes, sintering in particular, within the DFG SPP PiKo. The work has been published in several articles [11–13], in close collaboration by the groups of Luding, Staedler and Kappl. We focus here on the numerical models developed in this process; for details of the experimental work, see [11].

The discrete element method (DEM), here abbreviated as discrete particle method (DPM), is based on the contact forces and follows the motion of all particles in the system. Besides the repulsive/elastic-plastic and viscous forces, attractive forces due to cohesion still pose challenges. Of particular interest is dry cohesion due to van-der-Waals forces, which increases due to plastic (irreversible) deformation at the contacts [2, 3, 14, 15, 22, 25, 29, 31, 34, 35, 38, 41, 42, 44, 45, 50, 51]. Such forces are a source for agglomeration, sticking or caking, disturbing transport and storage of powders in many processes, and affecting the processes related to additive manufacturing. DPM has previously been shown to provide quantitatively accurate predictions [17, 30], if the microscopic contact laws are accurately calibrated. The understanding of particles in contact, by studying the mechanisms involved during contact and at separation (pull-off), was the main aim of most projects in PiKo. One result was to improve existing, or define new models or contact laws. Calibrating contact laws—either directly or indirectly, by contact or bulk measurements, involving experiments and simulations—was a central aim of various PiKo projects, e.g., for adhesive forces [19, 24]. However, taking experimental data for calibration is not trivial—not even for ideal spheres [11]; most powders are composed of micron-sized particles with irregular, sometimes fractal shapes [40]. An additional challenge for modelling sintering processes, is that micro-properties are not constant, but depend on the pressure and temperature applied to the particle bulk, and via force-chains to the single particle contacts. These dependencies are not well-known yet [11, 13, 29, 56].

We therefore approach the calibration process in two steps. In section "Contact Models", we present a general DPM contact model that takes into account elasto-plastic, adhesive and frictional forces, as well as time-, pressure- and temperature dependent effects, as relevant e.g., during sintering or additive manufacturing. In section "Experimental Calibration of the Elastic-Adhesive, and Frictional Forces", we show how to use existing and novel experimental methods to validate and calibrate this contact model; first, we calibrate the general properties, then we focus on the behaviour during sintering. The results of these experiments are presented and simulated in section "Initial Stage Sintering of Polymer Particles".

Contact Models

In this section, we review notation, kinematics, and basic contact mechanics for a two-particle contact in section "Contact Mechanics". Based on this, a general contact is proposed, in section "Contact modelling" accounting for adhesive, elasto-plastic, dissipative and frictional forces, and complemented by the new model for the time-, pressure-, and temperature-dependent formation of sinter necks in section "Sintering Forces".

Contact Mechanics

Notation

We denote the mass of particle i as m_i, its centre-of-mass, or position, $\mathbf{r}_i$, its velocity $\mathbf{v}_i$ and the angular velocity around its centre-of-mass $\boldsymbol{\omega}_i$ (Fig. 1).

The definitions of the contact overlap δ_{ij} and the unit normal at the contact $\hat{\mathbf{n}}_{ij}$ between two particles i, j depend on the shape and size of the particles. For contacts between two spherical particles i, j with radii r_i, r_j, the overlap is $\delta_{ij} = r_i + r_j - |\mathbf{r}_i - \mathbf{r}_j|$ and the unit normal $\hat{\mathbf{n}}_{ij} = (\mathbf{r}_i - \mathbf{r}_j)/|\mathbf{r}_i - \mathbf{r}_j|$. For contacts between a spherical particle i and a planar surface w, with outward unit normal $\hat{\mathbf{n}}_w$ and crossing the point $\mathbf{r}_w$, we define the unit normal $\hat{\mathbf{n}}_{iw} = \hat{\mathbf{n}}_w$ and the overlap as $\delta_{iw} = r_i - (\mathbf{r}_w - \mathbf{r}_i) \cdot \hat{\mathbf{n}}_w$.

We further define the corrected radius $r_{ij} = r_i - \delta_{ij}/2$, the contact point $\mathbf{c}_{ij} = \mathbf{r}_i - r_{ij}\hat{\mathbf{n}}_{ij}$, the branch vector $\mathbf{r}_{ij} = \mathbf{r}_i - \mathbf{c}_{ij}$, the surface velocity of particle i at the contact point $\mathbf{v}_i^c = \mathbf{v}_i + \mathbf{r}_{ij} \times \boldsymbol{\omega}_i$, the relative surface velocity at the contact $\mathbf{v}_{ij} = \mathbf{v}_i^c - \mathbf{v}_j^c$, the relative angular velocity $\boldsymbol{\omega}_{ij} = \boldsymbol{\omega}_i - \boldsymbol{\omega}_j$, and the effective mass $m_{ij} = m_i m_j/(m_i + m_j)$.

For readability, we omit the ij-subscripts in the following sections.

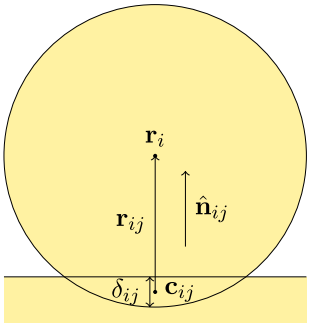

Fig. 1 Particle-wall contact

Decomposition of Contact Forces and Torques

Particles in DPM are assumed to be undeformable, but can slightly overlap. Thus, two particles interact via contact forces and torques acting at a single contact point, instead of a stress distribution over a contact area. These forces and torques, however, can be derived from integrating the stresses over the contact surface.

Integrating over the normal and tangential surface stresses yields the normal and tangential, lateral components of the contact force,

$$\mathbf{f} = f^{\mathrm{n}}\hat{\mathbf{n}} + \mathbf{f}^{\mathrm{l}}. \tag{1a}$$

Similarly, the torque around the particle's centre-of-mass can be decomposed into (*i*) a torque due to the tangential contact force, $\mathbf{r} \times \mathbf{f}^{\mathrm{l}}$, and (*ii*) remaining normal, $\mathbf{M}^{\mathrm{to}}$, and tangential, $\mathbf{M}^{\mathrm{ro}}$, components, yielding the total torque,

$$\mathbf{M} = \mathbf{r} \times \mathbf{f}^{\mathrm{l}} + \mathbf{M}^{\mathrm{ro}} + \mathbf{M}^{\mathrm{to}}. \tag{1b}$$

Objective Decomposition of Contact Velocities and Displacements

The decomposition by Luding [22], splits the relative translational and angular velocities and displacements into four components:
(a) The normal relative velocity,

$$v^{\mathrm{n}} = \mathbf{v} \cdot \hat{\mathbf{n}}, \tag{2}$$

(b) the lateral sliding velocity, due to tangential surface displacements at the contact,

$$\mathbf{v}^{\mathrm{l}} = \mathbf{v} - v^{\mathrm{n}}\hat{\mathbf{n}}, \tag{3a}$$

(c) the rolling "velocity" at which two surfaces roll over each other,

$$\mathbf{v}^{\mathrm{ro}} = r(\boldsymbol{\omega} \times \hat{\mathbf{n}}), \text{ and} \tag{3b}$$

(d) the torsion "velocity", measuring the normal relative angular velocity scaled by the effective radius,

$$\mathbf{v}^{\mathrm{to}} = r(\boldsymbol{\omega} \cdot \hat{\mathbf{n}})\hat{\mathbf{n}}. \tag{3c}$$

Each of these velocities is objective, meaning that the observer will measure the same velocities, even if (the frame of reference) is relocated by a finite translation and/or rotation, see Refs. [18, 22] for the general objectiveness of the rolling velocity. The normal relative velocity equals the time-derivative of the (normal) overlap,

$$\frac{d}{dt}\boldsymbol{\delta} = \mathbf{v}^{\mathrm{n}}. \tag{4}$$

Similarly, the other velocities are given by their respective rates of change of the displacements,

$$\frac{d}{dt}\boldsymbol{\delta}^{\nu} = \mathbf{v}^{\nu}, \quad \nu = \mathrm{l}, \mathrm{ro}, \mathrm{to}, \tag{5}$$

where, however, (elastic) displacements are set to zero at the beginning of a contact and the displacements have to be obtained by integrating the velocities over time. We assumed here that the normal vector $\hat{\mathbf{n}}$ is constant over time, which is the case for particle-surface contacts; for particle-particle collisions, the displacements are calculated such that the directions of $\boldsymbol{\delta}^{\mathrm{l}}$, $\boldsymbol{\delta}^{\mathrm{ro}}$ stay perpendicular, while $\boldsymbol{\delta}^{\mathrm{to}}$ stays parallel to the normal vector, see [22] for details.

Contact Modelling

Next, we propose an objective contact model based on the above considerations. The normal force f^n is described in section "Normal Contact Force", the tangential forces and torques in section "Tangential Forces and Torques".

Normal Contact Force

We use the model by Luding [22], where the normal force f^{n} is decomposed into a repulsive, dissipative, and adhesive component,

$$f^{\mathrm{n}} = f_{\mathrm{ep}} - \gamma^{\mathrm{n}} v^{\mathrm{n}} - f_{\mathrm{a}}. \tag{6}$$

The repulsive (elasto-plastic) force due to mechanical contact interactions, $f_{\mathrm{ep}} = k^{\mathrm{n}}(\delta - \delta_p)$, is discussed in different variants below. Note that the stiffness k^{n}, the plastic deformation δ_p, the dissipation γ^{n}, and the adhesive force f_{a}, are not necessarily constants; different dependencies have been proposed for different materials and conditions. The dissipative force, $-\gamma^{\mathrm{n}} v^{\mathrm{n}}$, reduces the relative velocity between the particles and thus results in (dynamic) energy dissipation, while the elasto-plastic force also dissipates energy under quasi-static load-unload cycles. The adhesive force can represent both dry and wet situations, where dissipation is taking place in the latter case, i.e., due to cutting of a liquid bridge [36, 39].

The simplest elastic-dissipative contact model assumes constant stiffness k^{n} and dissipation γ^{n}, without plastic deformation $\delta_p = 0$. The result is a simple, analytically tractable, contact model with simple physical characteristics, namely a velocity-independent duration of collisions and restitution coefficient [22, 39]. This model is used in section "Initial Stage Sintering of Polymer Particles", for simplicity, as basis, since the elastic-dissipative properties are likely not dominating the more complex sintering mechanisms; this way, one can focus on the effects of other elements of the model.

In section "Experimental Calibration of the Elastic-Adhesive, and Frictional Forces", where we measure the contact properties for all the different degrees of freedom, we account for the variable stiffness by applying Hertz' model for purely elastic contacts between spherical particles [16], $k^{\mathrm{n},H} = \frac{4}{3}E^* a$, where the effective modulus $E^* = [(1-\nu_i)/(2G_i) + (1-\nu_j)/(2G_j)]^{-1}$ is a combination of the shear moduli G_i, G_j and Poisson's ratios ν_j, ν_j of the two materials, and the radius of the contact area is approximated by $a = \sqrt{\bar{r}\delta}$ for $\delta \ll \bar{r}$, with $\bar{r} = 2r_i r_j/(r_i + r_j)$ the harmonic mean of the particle radii. We further use a variable dissipation coefficient according to [47], $\gamma^{\mathrm{n}} = 0.0062\sqrt{k^{\mathrm{n},H} m}$, which results in a constant restitution coefficient [21].

For larger deformations, we need to account for plastic deformations at the contact. This is done by introducing a plastic overlap, $\delta_{\mathrm{p}} \geq 0$, the overlap at which the normal contact force vanishes. The stiffness increases with the plastic deformation, due to the increased contact area, with $k^{\mathrm{n}} = k_{\mathrm{l}}$ for zero plastic overlap, and during loading, interpolating up to the maximum of $k^{\mathrm{n}} = k_*$ at $\delta_{\mathrm{p}} = \delta_*$. This is expressed as

$$k^{\mathrm{n}} = k_{\mathrm{l}} + (k_* - k_{\mathrm{l}})(\delta_{\mathrm{p}}/\delta_*)^{\psi}, \tag{7}$$

in [22], where the maximal previous overlap was used instead of the plastic overlap. At first, the power $\psi = 1$ was used due to lack of calibration data [22, 23]. It was generalised to arbitrary ψ during the DFG SPP PiKo, in order to account for a more general non-linearity of the elastic-plastic contact law [39] and to allow calibration of the contact model with experimental measurements for a wider class of materials and under extreme conditions like during tabletting. It also includes the traditional Walton model [52] with constant k^{n} for $\psi = 0$. For spherical particles, $\delta_* \approx r/6$ ensures that the maximum stiffness is reached when the solid volume fraction approaches unity, i.e. when all void space between the particles is filled [22].

The plastic overlap increases if a new maximum overlap is achieved, up to the limit of δ_*, or drops if $\delta < \delta_p$,

$$\delta_{\mathrm{p}} = \begin{cases} \frac{k^{\mathrm{n}} - k_{\mathrm{l}}}{k^{\mathrm{n}}}\delta & \text{if } k^{\mathrm{n}}(\delta - \delta_{\mathrm{p}}) \leq k^{l}\delta \leq k_*(\delta - \delta_{\mathrm{p}}), \\ \delta & \text{if } \delta < \delta_{\mathrm{p}}. \end{cases} \tag{8}$$

This ensures that the repulsive force vanishes for $\delta \leq \delta_p$. The reduction in plastic overlap during unloading allows for the complex, hysteretic reloading behaviour sketched in Fig. 2.

The adhesive force at $\delta = 0$ can be measured as the pull-off force f_{pull} required to detach a particle from a surface. To avoid an abrupt change of adhesive force when a contact opens, the adhesive force is modelled as

$$f_{\mathrm{a}} = \begin{cases} f_{\mathrm{pull}} & \text{if } 0 \leq \delta, \\ k_c\delta + f_{\mathrm{pull}} & \text{if } -f_{\mathrm{pull}}/k_c \leq \delta < 0, \\ 0 & \text{if } \delta \leq -f_{\mathrm{pull}}/k_c. \end{cases} \tag{9}$$

For simplicity, we use $k_c = k_{\mathrm{l}}$.

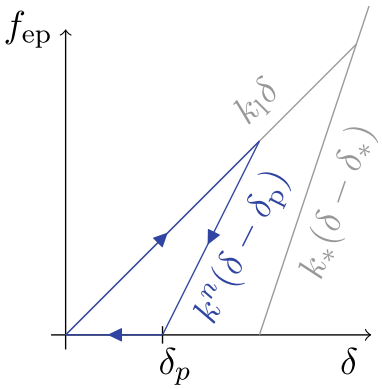

Fig. 2 Elasto-plastic repulsive force

Tangential Forces and Torques

The tangential sliding force and the rolling and torsion torques are assumed to resist the relative tangential and angular velocities, $\mathbf{v}^\nu$, and act against displacements, $\boldsymbol{\delta}^\nu$, with $\nu = \mathrm{l}, \mathrm{ro}, \mathrm{to}$. They can be modelled by coupling an elastic and a dissipative force,

$$\mathbf{f}^\nu = k^\nu \boldsymbol{\delta}^\nu - \gamma^\nu \mathbf{v}^\nu, \quad \nu = \mathrm{l}, \mathrm{ro}, \mathrm{to}. \tag{10a}$$

The rolling and torsion "forces" calculated here are not actual forces, but only used as intermediates to calculate the rolling and torsion torques,

$$\mathbf{M}^{\mathrm{ro}} = \frac{\lambda^{\mathrm{ro}}}{r}\mathbf{r} \times \mathbf{f}^{\mathrm{ro}}, \quad \mathbf{M}^{\mathrm{to}} = \lambda^{\mathrm{to}}\mathbf{f}^{\mathrm{to}}, \tag{10b}$$

where the length scales λ^{ro}, λ^{to} have to be specified.

Each of the three tangential forces/torques is assumed to have an *independent* yield criterion, where combined criteria are necessary for, e.g., the case of solid-bridges [4]. In the case of lateral slip this means: When the ratio of tangential to the nonadhesive normal force exceeds the static contact friction coefficient, $\mu^{\mathrm{l,s}}$, the contact surface yields until the ratio becomes smaller than or equal to the dynamic contact friction coefficient, μ^{l}. This is modeled by a yield criterion, truncating the magnitude of $\boldsymbol{\delta}^{\mathrm{l}}$ as necessary to satisfy

$$|\mathbf{f}^{\mathrm{l}}| \leq \mu^{\mathrm{l}}(f^{\mathrm{n}} + f_{\mathrm{a}}). \tag{11a}$$

The sliding friction coefficient μ^{l} is usually assumed to be constant (Coulomb type). While the static friction coefficient is generally larger than the dynamic friction coefficient, we assume for simplicity that $\mu^{\mathrm{l,s}} = \mu^{\mathrm{l}}$. Similarly, when the rolling or torsion torque-to-normal-force ratio becomes larger than the contact friction coefficient, μ^ν, the magnitude of $\boldsymbol{\delta}^\nu$ is cut as necessary to satisfy

$$|\mathbf{M}^{\nu}| \leq \mu^{\nu}\lambda^{\nu}(f^{\mathrm{n}} + f_{\mathrm{a}}), \ \nu = \mathrm{ro}, \mathrm{to}. \tag{11b}$$

Here, we assume the friction coefficients μ^{ν} and adhesive forces f_{a} to be constant for the sake of a simple contact model.

Different models have been presented in the literature for the stiffness and friction coefficients. For Hertzian contacts, see "Normal Contact Force" the Mindlin [27] model assumes a non-linear sliding force with a spring stiffness depending on the contact radius (and thus on the normal load).

$$k^{\mathrm{l,M}} = 8G^{*}a, \tag{12}$$

where $G^{*} = [(2-\nu_i^2)/G_i + (2-\nu_j^2)/G_j]^{-1}$. This contact model is a simplification of the contact model of Mindlin–Deresiewicz [28], implemented in [47], where a varying spring stiffness $k^{\mathrm{l,MD}}$ is used that depends on the contact history. Note that if the spring stiffness k^{ν} varies during tangential displacement, the tangential force has to be computed incrementally [47].

Sintering Forces

It remains to specify how changes in pressure and temperature can lead to a permanent agglomeration of the particles. All parameters of the contact model—and the particle density—may vary with temperature [23], but we neglect this effect here for simplicity. Temperature-assisted sintering is described on the micro-scale by the formation of sinter necks at inter-particle contacts, caused by viscous flow of the particles' raw material at temperatures above the glass transition [26]. Pressure, on the other hand, causes elasto-plastic deformation of the contacts, which also leads to flow and possibly agglomeration. When, both pressure and temperature are applied, the two effects combine. Modelling this has been a particular challenge to existing sintering models, see e.g. [29], where sintering is modelled as a purely viscous, non-elastic process. Such models can be adapted to model temperature-assisted sintering under constant pressure [35], but do so by gradually transitioning between viscous and elastic contact models.

Here, we present a contact model, first published in [13], that allows for the simultaneous simulation of temperature- and pressure-assisted sintering. We extend the elastoplastic contact model of [22], which accounts for the deformation due to pressure, and apply a temperature-dependent viscous deformation-rate to the plastic overlap δ_{p},

$$\dot{\delta}_{\mathrm{p}} = \frac{f_{\mathrm{n}}\bar{r}}{n f_{\mathrm{a}}\tau}\left(\frac{\bar{r}}{x}\right)^{n-1}. \tag{13}$$

where $x = \sqrt{2}a$ denotes the sinter neck radius, see Fig. 3. For two particles without compression ($f_{\mathrm{n}} = f_a$) and of high stiffness (for which the contact duration

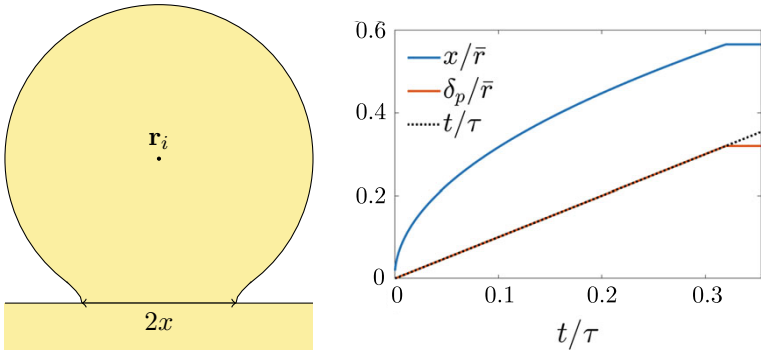

Fig. 3 (*left*) Sketch of sintered particle-wall contact; (*right*) contact radius x and plastic overlap for a particle-wall contact for $n = 1$, for the contact law used in section "Initial Stage Sintering of Polymer Particle". The neck radius plateaus when $\delta_\mathrm{p} = \delta_*$ is reached

$\sqrt{m/k} \ll \tau$), one can assume that $\delta = \delta_\mathrm{p}$, therefore the plastic overlap increases as $\delta_\mathrm{p}/\bar{r} = \sqrt[n]{t/\tau}$. Therefore, τ denotes the *sintering time scale* and n the *sintering power law exponent*. Such a law can be rigorously derived from the force laws derived in [1] for surface sintering, which yields an exponent $n = 3$. For $n = 1$, we obtain the well-known Frenkel law [9] for viscous sintering, for which $x/\bar{r} \approx \sqrt{\delta/\bar{r}} \propto \sqrt{t}$, see Fig. 3; the remaining particle properties, see section "Initial Stage Sintering of Polymer Particles", do not significantly influence the result. If the increase of the particle radius due to sintering would be taken into account, we obtain the modified Frenkel law derived in [33]; for more details, see [12, 13].

Experimental Calibration of the Elastic-Adhesive, and Frictional Forces

We introduce and apply nanoindentation-based testing techniques for characterising the elastic, adhesive, and frictional forces of individual particle-surface contact, see Fig. 7. For brevity, we only provide a short description of the materials and experimental methods used. Further details can be found in [11] (Fig. 4).

Test Objects

Surfaces and Spherical Particles

The substrate material used was a single-crystalline Si(100) wafer, supplied by Siegert Wafer GmbH, Aachen. Surface topography changes of these samples were

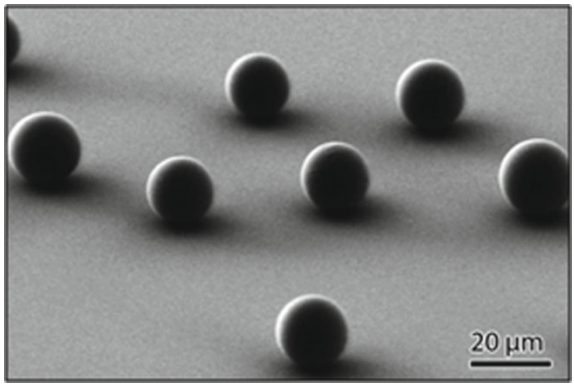

Fig. 4 Borosilicate glass spheres featuring a diameter of about 17 µm on a Si substrate

achieved through a slow etching process using H_2 plasma. Two different microwave powers (1600 and 1800 W) are used to sustain the plasma. The etching period was 20 min for all samples. This treatment leads to a variation in surface roughness due to the different etching efficiency of the H_2 plasma with different microwave power. Surface roughness was measured using atomic force microscopy, see Fig. 5 and Table 2.

A Focused-Ion beam (FIB) system (FEI Helios 600) was used to create rail-structure silicon samples (see Fig. 7), featuring a length of 100 µm and rail inclinations of 25°, 45° and 60°, respectively. Depth and width of the rails were chosen in such a way that the centre of mass of the particles was situated 1 µm below the wafer's surface level. This design effectively keeps the particles inside the rail during an experiment.

Regarding model particles, guided by the work of van Zwol et al. [49] we decided in favour of borosilicate glass beads (Duke Standards 9020).

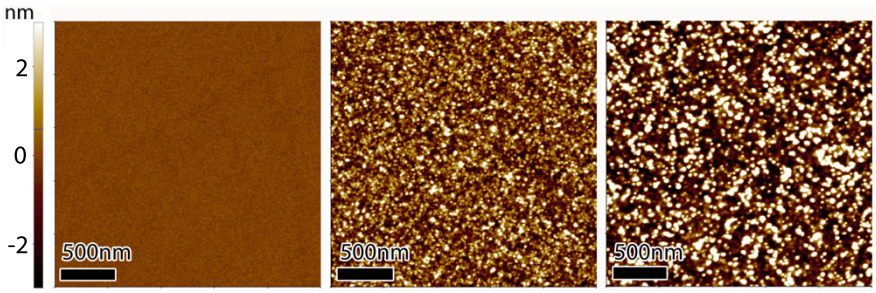

Fig. 5 AFM topography images of the Si surfaces clearly show the roughness change after MWCVD H_2 etching with 1600 W (middle) and 1800 W (right) power. The RMS variations of the surface heights are 0.3 ± 0.1 nm, 1.5 ± 0.2 nm and 2.7 ± 0.4 nm (upper panels, left to right)

Colloid and Other Probes

AFM colloidal probes were prepared by attaching the borosilicate glass spheres to Mikromasch NSC12 tip-less AlBS cantilevers with epoxy (Araldite 10 min, 2 components). The radii of the colloid probes and the quality (clean contact area) were determined by using scanning electron microscopy. In order to prepare colloid probes for the scanning nanoindenter (TriboIndenter, Hysitron Inc.) used in this work, the FIB was employed to create appropriate cavities into the apex of a commercially available diamond cube corner tip (Hysitron Inc.), see Fig. 7. Subsequently, the borosilicate spheres were fixed to this holder by means of a small amount of photosensitive acrylate-based adhesive glue (DIC Europe GmbH). A flat end diamond indenter (20 μm diameter, Hysitron Inc.) and non-glued spheres were utilised to sample rolling and torsional friction, as detailed in [10].

Normal Tests

Figure 6 shows a load-displacement curve obtained by using the nanoindenter colloid probe on a silica substrate. Elastic modulus and Poisson's ratio are assumed to be 71 GPa and 0.17 for both sphere and surface (Table 1), respectively. A simple Hertzian fit with a slightly larger radius of 9 μm was able to accurately reproduce the experimental data. The slightly stiffer response has to be attributed to a combination of surface roughness (about 0.7 ± 0.1 nm) and non-sphericity (i.e. local variation in actual radius).

According to Tabor [43], the yield stress can be approximated as one third of the hardness. For the silica surface used in this experiment, a measured hardness of 9 GPa results in a yield stress of 3 GPa, slightly above the maximum contact pressure of 2.8 GPa acting at the contact area with a flat substrate, based on the highest normal loads used in our sliding and rolling experiments, $f^{\mathrm{n}} \leq 3000\,\mu\mathrm{N}$. Therefore, with silica being the weakest material in this study, we have a predominantly elastic Hertzian contact in all experimental settings presented here.

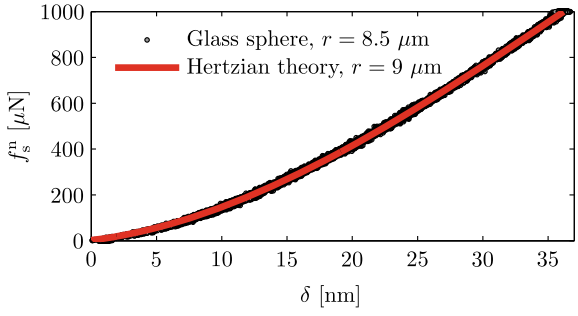

Fig. 6 Normal load $f_{\mathrm{s}}^{\mathrm{n}}$ versus displacement curve δ. The red line shows a fit with Hertzian theory by assuming a radius of 9 μm, with materials from Table 1

Table 1 Material properties for substrates, particle and probes used for normal, sliding, rolling and torsion tests

	Substrate 1	Substrate 2	Indenter	Particle
Material	Si(100)	Fused quartz	Diamond	Borosilicate
Young's modulus	$E_s = 179\,\text{GPa}$	$E_s = 71\,\text{GPa}$	$E_i = 1140\,\text{GPa}$	$E = 71\,\text{GPa}$
Poisson's ratio	$\nu_s = 0.25$	$\nu_s = 0.17$	$\nu_i = 0.07$	$\nu = 0.17$
RMS roughness Δ (nm)	See Table 2		4.0 ± 1.0	0.7 ± 0.1
	(For sliding/rolling/rail)	(For normal testing)	(For rolling/rail)	$R = 8.5\,\mu\text{m}$

The adhesion measurements are summarised in Table 2. The measured pull-off forces, f_{pull}, decrease with increasing RMS roughness. As surface chemistry (amorphous SiO_2) and measurements conditions are kept constant, this finding is directly related to a diminished real contact area due to the roughness. The results are in good agreement with recent experimental results of Liu et al. [20], who studied the correlation between adhesion, tip radius and surface roughness in more detail.

Sliding Tests

In order to characterise the sliding friction of the particles in the predominant elastic contact regime, nanoindenter colloid probe tips have been used according to the schematic given in Fig. 7.

The sliding friction tests were performed in a nanoindentation-based setup using a TriboIndenter in combination with a Performech upgrade (Hysitron Inc.). The actual tests to characterise sliding friction were carried out at room temperature and $30 \pm 5\%$ relative humidity in a friction loop fashion, which is a common technique in the AFM community. In this case the probes have been scratched back and forth over a distance of $2\,\mu\text{m}$ at a constant normal load and a speed of $1\,\mu\text{m/s}$ under load control. The normal load was varied between 3 and $100\,\mu\text{N}$; five spheres were utilised probing each load five times at different surface spots for all Si surfaces, respectively. In turn, the corresponding absolute value of lateral force for each test was evaluated by a lateral displacement sensitive averaging of the difference in measured lateral force for forward and backward movement divided by two. In order to avoid artefacts originating from a change in the movement direction, only the central micron range of the friction loop was taken into account.

The results of the sliding friction tests are summarised in Fig. 8 left. A linear dependence between the measured lateral force f_s^l and the applied normal load f_s^n can be seen. The linearity of these three curves indicates that the modified Coulomb friction law (11a) holds for the given experimental conditions. A linear fit of the data yields the sliding friction coefficient μ^l along with an offset, which can be related to the adhesion f_a^n between the contact partners. The results from the linear regression are summarised in Table 2.

Table 2 Contact properties for sliding and rolling tests on different rough Si surfaces and effective friction values for rolling/torsion tests

Substrate 1 surfaces	Untreated	Etched (1600 W)	Etched (1800 W)	Section
RMS roughness Δ (nm)	0.3 ± 0.1	1.5 ± 0.2	2.7 ± 0.4	section "Test Objects"
Peak-to-valley (nm)	1.0 ± 0.1	10.5 ± 0.7	14.8 ± 1.0	
AFM pull-off force f_{pull} (μN)	3.2 ± 0.3	2.7 ± 0.3	1.9 ± 0.3	section "Sliding Tests"
Sliding friction $\mu_{\text{s}}^{\text{l}}$	0.23 ± 0.005	0.53 ± 0.005	0.65 ± 0.014	
Sliding adhesion f_{a}^{l} (μN)	12.00 ± 1.20	4.45 ± 0.55	7.76 ± 1.17	
Rolling fr. $\bar{\mu}^{\text{ro}}$ for $\bar{\lambda}^{\text{ro}} = \bar{r}$	$(7.9 \pm 0.3) \times 10^{-4}$	$(4.6 \pm 0.2) \times 10^{-4}$	$(3.5 \pm 0.3) \times 10^{-4}$	section "Rolling Tests"
Ro. adh. $\bar{f}_{\text{a}}^{\text{ro}}$ for $\bar{\lambda}^{\text{ro}} = \bar{r}$ (μN)	571.4 ± 56.1	1398.0 ± 82.7	2029.4 ± 149.2	
Rolling fr. $\bar{\mu}^{\text{ro}}$ for $\bar{\lambda}^{\text{ro}} = \bar{a}$	$(7.6 \pm 1.0) \times 10^{-3}$	$(1.8 \pm 0.7) \times 10^{-3}$	$(1.7 \pm 1.3) \times 10^{-3}$	
Ro. adh. $\bar{f}_{\text{a}}^{\text{ro}}$ for $\bar{\lambda}^{\text{ro}} = \bar{a}$ (mN)	2.6 ± 0.6	13.5 ± 5.6	12.6 ± 11.0	
Rail inclination (°)	25 ± 0.5	45 ± 0.5	65 ± 0.5	
RMS roughness Δ (nm)	2.5 ± 1.0	3.6 ± 1.4	4.8 ± 2.0	section "Test Objects"
Rail friction coeff. μ^{rail}	$(1.58 \pm 0.02) \times 10^{-3}$	$(2.42 \pm 0.09) \times 10^{-3}$	$(3.34 \pm 0.19) \times 10^{-3}$	section "Combined Rolling and Torsion Tests"
Rail adhesion $f_{\text{a}}^{\text{rail}}$ (μN)	173.4	57.8	191.3	
Torsion fr. $\mu_{\text{t}}^{\rightarrow}$ for $\lambda^{\rightarrow} = r$		$(5.6 \pm 0.5) \times 10^{-3}$		
Torsion fr. $\mu_{\text{t}}^{\rightarrow}$ for $\lambda^{\rightarrow} = a$		$(6.4 \pm 1.2) \times 10^{-2}$		

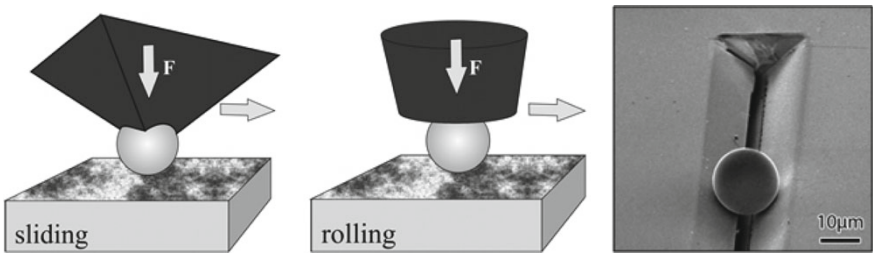

Fig. 7 Schematic of the test setups for sliding (left), rolling (middle) and rolling-torsion (right) measurements of individual fixed micron-sized borosilicate particles on a Si substrate

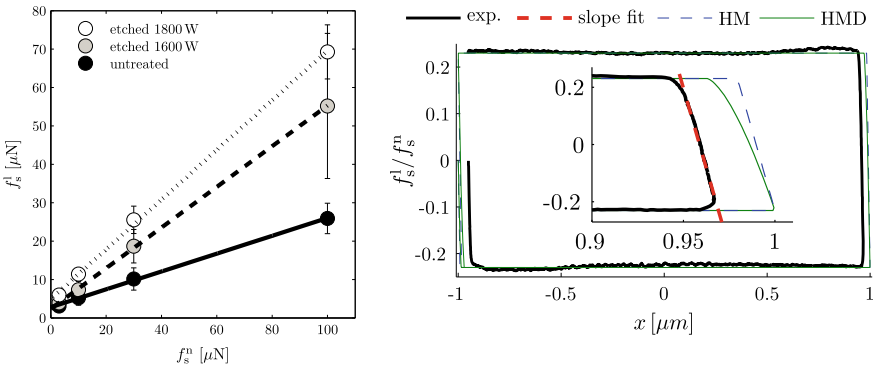

Fig. 8 (*left*) Measured lateral force f_s^l versus normal load f_s^n for sliding friction measurements. Lines represent simple linear fits, from which f_a^l, μ^l are extracted. (*right*) Shear force against displacement for the sliding experiment with the untreated substrate and $f_s^n = 100\,\mathrm{mN}$ (thick black line). This is compared to DEM simulations using Hertz-Mindlin (blue dashed line) and Hertz-Mindlin–Deresiewicz (green line), with a fitted shear modulus of $G^{*,\mathrm{fit}} = 1.21\,\mathrm{GPa}$ (thick red dashed line)

The larger values of sliding adhesion forces compared to the normal adhesion measurements potentially stem from the differences in the dynamics of the process that detaches micro-asperities from a surface and the process that initiates new contacts during shear of the sphere along the substrate.

Comparison to Model

For the sliding case, shown in Fig. 7 (left), the particle is attached to the indenter and thus moved with the same velocity as the indenter. The resulting shear force versus displacement curve is compared to an experimental friction loop in Fig. 8. The friction loop shows nearly linear elastic behaviour for short intervals after the reversal point (where the velocity switches directions). For the elastic behaviour, the force balance yields that the slope of the shear force versus displacement curve at the load reversal point equals the negative sliding spring stiffness, $d\, f_{\mathrm{el},i}^l / dx = -k^l$. For both the linear Mindlin and the nonlinear Mindlin–Deresiewicz [28] models, a stiffness of $k^l = 8G^* a$ holds true at the reversal point.

The slope fitted to the experimental friction loop plotted in Fig. 8 yields $k^{\mathrm{l,fit}} = 2.219\,\mathrm{kN/m}$ for a normal load of $f_{\mathrm{s}}^{\mathrm{n}} = 100\,\mu\mathrm{N}$; this yields $G^{*,\mathrm{fit}} = k^{\mathrm{l,fit}}/(8a) = 1.36\,\mathrm{GPa}$, which is much smaller than the value calculated from the material parameters in Table 1 of a perfectly flat borosilicate sphere and a silicon substrate ($G^* = 11.87\,\mathrm{GPa}$). This result can be due to the nano-structure of the surfaces; however, it is difficult to interpret as the elasticity of the nanoindenter setup could possibly influence the slope observed in the friction loop.

After the sliding spring yields, the magnitude of the sliding force remains constant at $\mu_{\mathrm{s}}^{\mathrm{l}}|f_{\mathrm{s}}^{\mathrm{n}}|$. Fitting the experimental results for the untreated surfaces shows a constant friction coefficient $\mu_{\mathrm{s}}^{\mathrm{l}} \approx 0.23$. A linear fit of the lateral force against the contact area, $f^{\mathrm{l}} \propto \pi a^2 \propto (f^{\mathrm{n}} + f_{\mathrm{a}}^{\mathrm{n}})^{2/3}$, as suggested in [48], did not produce good, consistent results. For higher roughness, and a peak at the transition from the elastic to the yielding sliding force (not shown) suggests that the static sliding friction coefficient is higher than the dynamic one, however, this will not be discussed further here.

Rolling Tests

The nanoindentation test setup for the measurement of rolling friction of the microspheres is significantly easier compared to the sliding case. The spheres are first placed on the surface, then contacted with a flat end diamond indenter, carefully positioning the indenter tip onto the apex of the particle.

Preliminary test results with single scratch length of about 10 μm and a speed of 1 μm/s under load control, showed that a certain threshold [37] or rolling resistance moment [6, 32] was necessary to initiate particle rolling. In our case, the rolling of particles, i.e. a change in position detected by optical microscopy, was only observed for normal loads larger than 100 μN.

Based on these results, a minimum normal load of 100 μN was selected for all rolling tests presented here to ensure rolling characteristics of the corresponding contact behavior. This 100 μN force to overcome the rolling resistant moment, was chosen independently of the load regime used in sliding tests. Again, in order to improve the reliability of the results, five beads were used for testing and each measurement, i.e. applied normal load, was taken five times for all Si surfaces, respectively.

Figure 9 shows the results of the rolling experiments. The mean rolling friction coefficient $\bar{\mu}^{\mathrm{ro}}$ was extracted from the friction loop data, as in the sliding experiments. The measured lateral force signals are 2–3 orders of magnitude smaller for rolling compared to sliding tests, which confirms that the particle is rolling over the surface. Surprisingly, in contrast to the sliding data, $\bar{\mu}^{\mathrm{ro}}$ decreases with increasing surface roughness, while the intercept with the abscissa shifts to the left, i.e., rolling adhesion $\bar{f}_{\mathrm{a}}^{\mathrm{ro}} \gg f_{\mathrm{a}}^{\mathrm{l}}$ increases with surface roughness. This suggests that a simple interpretation of this intercept as a measure of the normal adhesion force between the contacting partners is not straightforward in the case of a rolling contact.

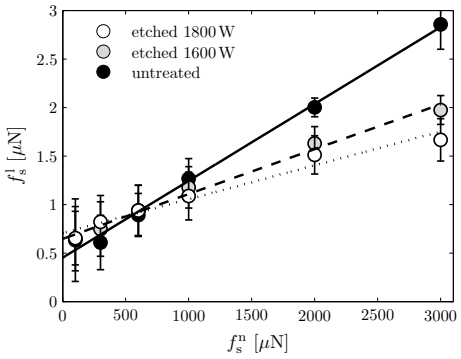

Fig. 9 Resulting lateral force f_s^l versus normal load f_s^n for rolling friction measurements. The lines represent simple linear fits to the corresponding data sets

Ideally, a non-adhering rolling sphere contacts with the underlying surface at only one point, which would result in a zero rolling friction since no torque can be created by a point contact. In our system, the finite contact surface, involving many single asperities on the sphere as well as on the substrate surface, leads to a non-zero rolling resistance due to various (three at least) dissipative phenomena. Rolling is a continuous generation of new contact area at the front and a continuous contact detachment at the rear of the contact (viewed in rolling-direction of the sphere). During this process, multiple surface mechanisms can dissipate energy [11]. Therefore, rolling friction appears to be attributable to various combinations of viscous, wet, and plastic effects at the individual asperities.

Analysis of the Rolling Measurements

An analysis of the forces relevant in the rolling experiment reveals that

$$f^l = \frac{\bar{\mu}^{ro}\bar{\lambda}^{ro}}{\bar{r}}(f^n + \bar{f}_a^{\,ro}), \tag{14}$$

where the bar denotes mean values for the two different surfaces.

Thus, the good approximation by a linear fit seems to suggest that the length scale λ^{ro} is proportional to the particle radius. The measured coefficients can be found in Table 2 for $\bar{\lambda}^{ro}=\bar{r}$ and $\bar{\lambda}^{ro}=\bar{a}$, where the contact radii been obtained using (2.2.1) and the data in Table 1.

In both cases, the rolling adhesion force, f_a^{ro}, is much higher than the pull-off force f_a^n, as the rolling friction appears to be large even for zero normal load. As discussed above, μ_s^l increases with higher surface roughness while $\bar{\mu}^{ro}$ decreases. These results show that $\bar{\mu}^{ro}$ is dominated by surface and interfacial forces such as *e.g.* water films while μ_s^l is dominated by mechanical frictional stick slip effects at asperities.

Combined Rolling and Torsion Tests

In combination with appropriate rail systems, the strategy to probe rolling friction, which has been introduced above, can also be exploited to study a combination of rolling and torsional friction. As far as the authors are aware, no scanning probe based technique has been proposed so far that would allow for the exclusive evaluation of torsion friction.

In order to access the combination of both mechanisms, we utilised Si-based rail structures featuring rail angles of 25°, 45° and 60°. Higher rail angles lead to an increased influence of the torsional contact mode.

Borosilicate spheres are placed inside the rails by AFM-based positioning (Fig. 7). In analogy to the rolling tests, the individual particles inside the rails are contacted and probed with a flat end diamond indenter. Careful positioning of the indenter tip with respect to the particle as well as alignment of the rail with regard to the scratch axis (movement direction) of the instrument are crucial.

The effect of scratch velocity can be considered negligible, since the results of the rolling test did not change while varying velocity from 1, 0.1 to 0.01 µm/s inside the rail system.

To estimate the rolling friction in the following rail experiments, both friction factor and rolling adhesion are fitted against the RMS roughness of the substrate, Δ, as an exponentially decaying value, $\bar{\mu}^{\mathrm{ro}} = b + c\exp(-\Delta/d)$, and $\bar{f}_{\mathrm{a}}^{\mathrm{ro}} = b' - c'\exp(-\Delta/d')$. with $b = 0.0002859$, $c = 0.0006475$, $d = 1.1548\,\mathrm{nm}$ and $b' = 3.046\,\mathrm{mN}$, $c' = 2.907\,\mathrm{mN}$, $d' = 1.5216\,\mathrm{nm}$, as shown in Fig. 10. The rolling friction factors in the rail experiments in section "Combined Rolling and Torsion Tests" are then assumed to satisfy the friction factors fitted to the rail roughness, see Table 2.

Experimentally, a controlled particle surface motion is possible by means of a Si based rail system featuring different inclinations. In the rail system, a controlled particle surface motion is possible, which results in an effective friction coefficient with contributions from both torsion and rolling resistance.

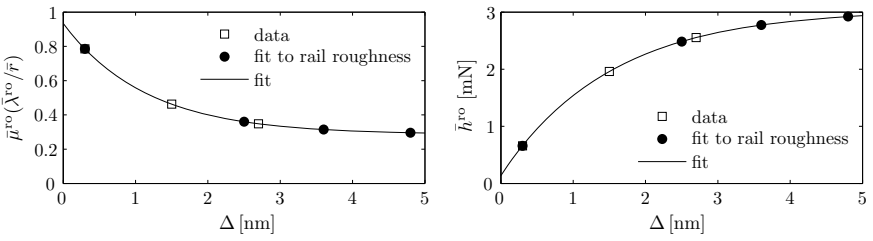

Fig. 10 Fit of the rolling friction coefficient $\bar{\mu}^{\mathrm{ro}}$ (top) and the rolling adhesion force $\bar{f}_{\mathrm{a}}^{\mathrm{ro}}$ (bottom) as functions of RMS roughness. This fit is used in section "Combined Rolling and Torsion Tests" to estimate the rolling friction in the rail experiments, based on the RMS roughnesses of the rail surface (dots)

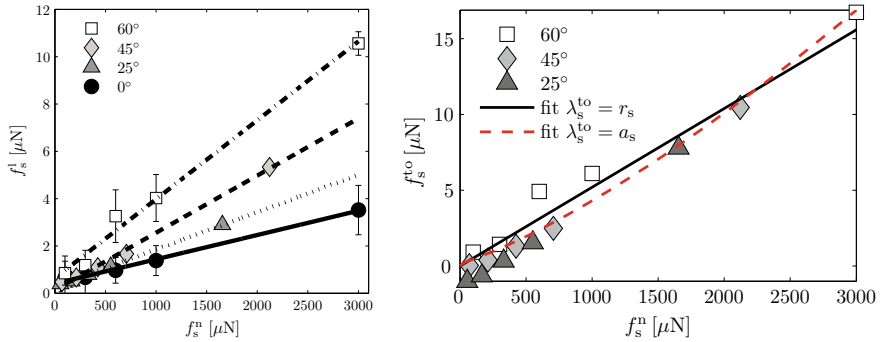

Fig. 11 (*left*) Resulting lateral force f^l versus effective normal load f_s^n for the rail system with different rail inclinations of 0°, 25°, 45° and 60°. All data sets are fitted with a linear relation. (*right*) Torsion contribution to the lateral force f_s^{to} versus effective normal load f_s^n. All data sets are fitted to Eq. (15); lines show fits of $\lambda_s^{to} = r_s$ (solid line) and $\lambda_s^{to} = a_s$ (dashed red line)

Fig. 11 shows the effective lateral forces, f^l, and normal loads, f^n, at the substrate contacts, which are calculated from the measured lateral force, f_i^l, and the applied normal load, f_i^n.

All results follow linear trends, confirming a modified Coulomb law, but the slopes, which are the effective friction coefficients μ^{rail}, show a clear correlation with increasing inclination of the rail, which will be further analysed in section "Analysis of Combined Rolling and Torsion".

The intercepts of the trend lines with the horizontal axis, taken as the values of rail adhesion, h^{rail}, are lower than for pure rolling. This suggests that adhesion plays a less dominant role during the combines rolling/torsion motion than for pure rolling on a plane surface.

Even though the experimental results presented up to now provide evidence of an increased effect of torsion with increasing inclination, a deeper insight into appropriate contact models is necessary to understand the evolution of the effective friction coefficient, μ^{rail}, with respect to inclination. In the following section, focusing on contact models and simulation, among other considerations, we strive to quantify the impact of rolling and torsional friction seen here.

Analysis of Combined Rolling and Torsion

An analysis of the forces relevant in the rail experiments [11] allows us to predict the rolling contribution to the lateral force measurement, and thus to extract the torsion component. This is plotted in Fig. 11.

The torsion friction shows an almost constant slope, which can be fitted by

$$\mu_s^{to} = 0.0056 \text{ for } \lambda^{to} = r, \tag{15a}$$

and

$$\mu_s^{to} = 0.064 \text{ for } \lambda^{to} = a. \tag{15b}$$

Both fits, plotted in Fig. 11, agree well with the data. Thus, the measurements are not able to distinguish if the torsion friction factor is independent of the normal force or scales with the (normal-force dependent) contact radius. The measured coefficient is about seven times smaller than the predicted value of $\mu_s^{to} = (2/3)\mu^1$ for $\lambda_\alpha^{to} = a_\alpha$, unless a smaller effective radius is used. A more detailed study with different particle radii is necessary to find correlations with either particle or effective contact radii.

Initial Stage Sintering of Polymer Particles

Here, we summarize experimental results on a thin bed of particles, heat-sintered but not fully melted [13]; its elastic properties are measured using a nanoindenter, which allows the calibration of the plastic deformation model for the forming and evolution of the sinter necks during time.

Preparation of Particles and Samples

Polystyrene spheres featuring nominal particle radii of 0.25, 0.5, 0.75 and 2 μm, molecular weights (M_w) of 111–312 kg/mol, and a glass transition temperature T_g of 94–99 °C were synthesised by dispersion polymerisation as reported in Zhang et al. [55] and stored in aqueous solution. For each particle radius, multi-layer films (<30 particle diameters) were realised by placing 10 ml of a particle suspension (1:1 volume ratio, PS particle:ethanol) on an oxygen-plasma hydrophilised glass substrate and dried for at least 24 h in air. Sintering was carried out in air on a heating stage at temperatures of 90, 95, 100, 105 and 110 °C. The rate of temperature change was set to be 15 °C/min during heating. Holding periods of 20, 40, 60, 90, 120 and 180 s were set at each temperature for each particle radius, respectively. After sintering, the samples were quickly cooled down to room temperature. The resulting average layer thickness reduced by up to 50% as the sintering temperature increases from room temperature to 110 °C.

Characterization of Microstructure by Slicing

The sintered PS particle layers were coated with a 100 nm Pt layer. A focused-ion beam combined with a scanning electron microscope (FIB/ SEM, Nova 600 Nanolab, FEI, USA), was then used for sectioning and imaging sequential 2D cross-sectional surface images, see Fig.12. A protective Pt layer of 1 μm thickness and $12 \times 8\,\mu m^2$ area was deposited on the sectioned sample. A volume of $12 \times 8 \times 6\,\mu m^3$ was milled slice-by-slice with 20 nm distance between two consecutive images. The actual 3D structures of the sintered films were reconstructed based on the as-recorded stacks

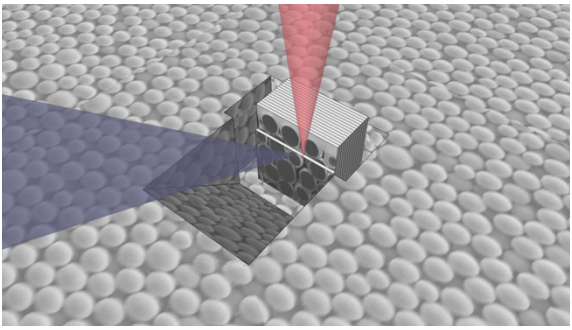

Fig. 12 Sinter bed sectioned via FIB/SEM for 3D reconstruction

of images using Amira 4.1 (Visage Imaging, San Diego, USA). The reconstruction process involved (i) alignment of the images, (ii) re-sampling and (iii) segmentation. The radius of at least 12 particles as well as the mean neck radius x was determined for each sintered sample.

Nanoindentation and Confocal Microscopy

Nanoindentation measurements were performed with an MFP NanoIndenter (Asylum Research, Santa Barbara, CA, spring constant $k = 2390$ N/m) equipped with a spherical ruby indenter of diameter $d = 127\,\mu$m. Indentations were performed in load-controlled mode. The applied load varied between 1 and 4 mN with loading rates between 200 and 800 μN/s. Each sample was tested at least at 12 individual positions. The reduced elastic modulus (E_{red}) for each sample was obtained from the unloading portion of the load-displacement curve using the Oliver and Pharr method with a spherical area function [7].

The nanoindenter was then placed on the sample stage of a custom-built laser scanning confocal microscope (LSCM), which has the capability to measure in situ the real-time deformation within the sintered particle layers during nanoindentation. The ruby sphere was indented into the sintered fluorescently labelled PS particle film in displacement-controlled mode with a maximum displacement of 5 μm, while the structure was imaged by LSCM. For the LSCM imaging, the sintered films needed to be submerged in a liquid that matches the refractive index of polystyrene (Cargille Laboratories, USA).

Mechanical Properties

After sintering of the PS particles samples under varying temperature-, size- and time-conditions, different densifications of the powder layer are obtained. It was found that the reduced elastic modulus (E_{red}) of each sintered film increased by a

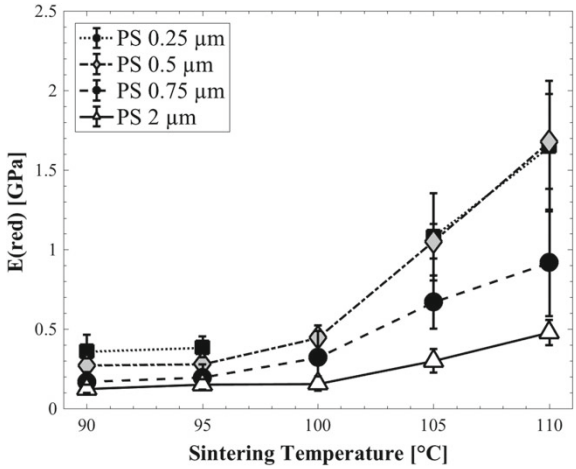

Fig. 13 Mechanical properties of PS multilayers with particle radii of 0.25–2 µm sintered for 60 s. E_{red} increases with the densification of the porous solids ($T > T_g$) which increases with decreasing particle size

factor of max. 6 for sintering temperatures above T_g as the sintering time increased from 20 to 180 s [12], while E_{red} also correlates strongly with the porosity of the film.

According to Mazur et al. [26], particles smaller than a certain limiting radius, r_{crit}, are predicted to sinter to uniform density regardless of the Newtonian viscosity. Consequently, the contact area initially grows much faster for particles with radius $r < r_{crit}$ than predicted by the classical sintering models [9, 33], which neglect the contribution of surface forces as well as the resultant plastic and elastic contact deformation in the early stages of sintering. Assuming an initial packing fraction of 58%, a critical particle radius of $r_{crit} = 1.055$ µm for sintering of PS particles is obtained.

Figure 13 shows E_{red} plotted against sintering temperature for layers made from PS particles with varying radii from 0.25 to 2 µm. Indeed, particles with $r \leq 0.5$ µm show a higher E_{red} compared to the larger particles, even for temperatures below T_g. This hints at an additional contribution of surface force and contact deformation, which leads to faster sintering in the initial stage. The variation of E_{red} (decrease) with particle size is a strong indication that there is a transition from sintering dominated by contact deformation for $r < r_{crit}$ to sintering dominated by viscous flow for $r > r_{crit}$. Consequently, larger particles require higher sintering temperatures and times to show the same mechanical properties as smaller particles.

In addition, in-situ real-time deformation within the sintered particle layers during nanoindentation was studied with the help of confocal microscopy. Cross-sectional xz-plane LSCM images for (a) not sintered films and films sintered at (b) 90 °C, (c) 100 °C and (d) 110 °C, all for 60 s, at maximum indentation depth, are shown in Fig. 14.

While the displacement of 5 µm is reached without exceeding the maximum force of the nanoindenter in case of Fig. 14a, b, the samples above T_g (Fig. 14c, d) show a smaller indentation depth at maximum load, due to a higher E_{red} of the porous sintered

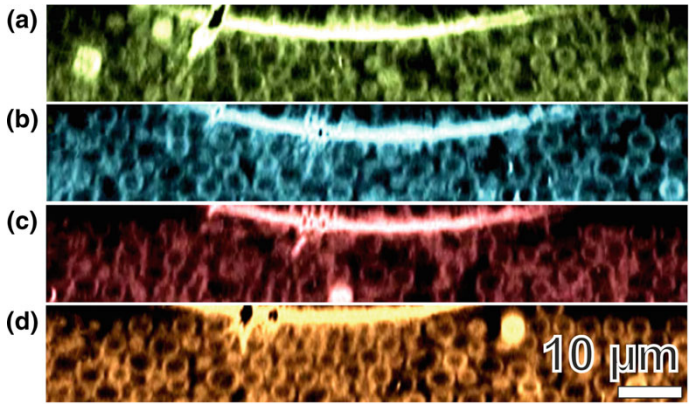

Fig. 14 LSCM image (xz plane) during indentation with a spherical tip for **a** not sintered PS multilayer film, **b** sintered at 90 °C for 60 s, **c** sintered at 100 °C for 60 s, and **d** sintered at 110 °C for 60 s. The maximum indentation decreases from (**a**) to (**d**) with increasing stiffness of the sample

layer. A plastically deformed region is observed after indentation for samples in Fig. 14a–c. The sample sintered at a temperature of 110 °C has a nearly fully elastic, reversible response. Such behavior can be attributed to a strong interconnection of the particles by sufficiently strong sintering necks.

Simulation Setup

Finally, we look at the analysis of the FIB/SEM data. A representative plot of the time-dependent increase of the sintering neck radius x at 110 °C for PS particles with radius of 1.5 µm is shown in Fig. 16, showing the increasing mean sinter neck radius as a function of time. We use this data to calibrate our sintering contact model, presented in section "Sintering Forces".

We model the sintering and indentation process with discrete particle simulations, using a small cubic domain of 60 µm, with a flat base wall and periodic boundary conditions in both width and length. We introduce 2178 particles of radii $1.35\,\mu\text{m} < r < 1.65\,\mu\text{m}$, producing a particle packing about 5 particle diameters thick (see Fig. 15). To simulate sintering in a reasonable amount of time steps, the collision time is scaled up to $t_c = 5$ ms, which is still several orders of magnitude smaller than the time scales of gravity, sintering, and indentation. Therefore, using such artificially soft particles has little effect on the results. The packing is sintered using a sintering time scale of $\tau = 666$ s and $n = 1$ (thus assuming viscous sintering) to match the experimental results. Adhesive van-der-Waals forces were modelled as $f_a = (1.2\,\mu\text{N/m})\bar{r}$, see [9]. The restitution coefficient was chosen as 0.5 to determine the stiffness and dissipation parameters with the goal to quickly dissipate velocity fluctuations; for the plastic regime, the maximum unloading stiffness was set to $10k_1$.

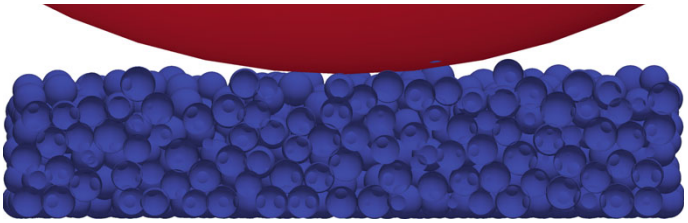

Fig. 15 Vertical cut through the centre of the simulated layer during indentation

Comparing the simulated forces on the nanoindenter with the experimental results displays a rich phenomenology, qualitatively simular in experiments and simulations. However, a detailed discussion is beyond the scope of this paper, and the quantitative calibration of the model still requires further research. Nevertheless, next we extract the typical sintering neck radius from experiments and compare it with different models.

Sinter Kinetics

We plot the simulation results for various models together with the experimental results in Fig. 16, as obtained with 3D reconstruction. The experiments show a higher growth rate in the early stages of sintering compared to the prediction of the classical sinter models of Frenkel [9] and the modified Frenkel model [33]. The simulation of viscous sintering ($n = 1$, $\tau = 666\,\mathrm{s}$) underpredict the experimental data while agreeing well with the Frenkel and modified Frenkel model, up to the point where the majority of contacts reach the maximum plastic overlap ($t > 120\,\mathrm{s}$). Simulations

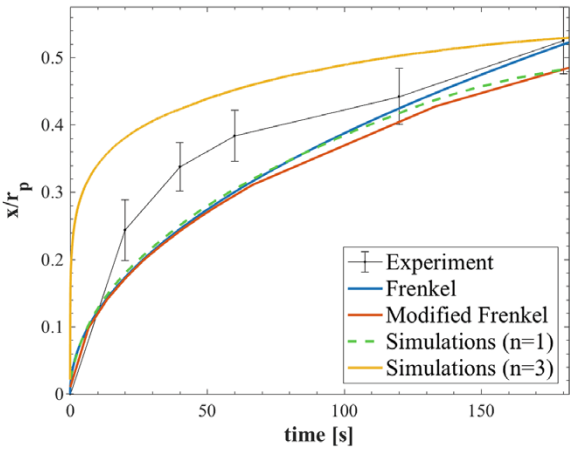

Fig. 16 Sintering kinetic of PS particle multilayer ($\mathbf{r}_\mathrm{p} = 1.5\,\mu\mathrm{m}$) at 110 °C compared with Frenkel model (blue line), modified Frenkel model (red line), and simulations of viscous sintering ($n = 1$, green line) and surface sintering ($n = 3$, orange line)

using the surface sintering model ($n = 3$, $\tau = 110\,\mathrm{h}$) systematically over-predict the early-stage sintering rate up to about $t > 180\,\mathrm{s}$. This indicates that viscous sintering is aided by an additional contribution of surface forces to the sintering process, but is not as strong as predicted by the extreme model with $n = 3$ which assumes ideal surface sintering.

Summary and Conclusions

This chapter begins with a short literature overview before the basics of contact models that involve pressure-, rate/time- and temperature-dependence are given. The model has some parameters that can be either directly or indirectly measured or calibrated experimentally. The former was carried out first, but only for well-defined spherical particles. Secondly, the temperature-driven growth of sinter necks was measured and compared to various models to indirectly determine the model and its parameters.

The direct measurements of the **pressure-dependence of contacts**—for all degrees of freedom in the relative motion of very small particles, such as normal adhesion and elasticity, sliding, rolling and torsion friction—was made possible by a relatively simple, but novel, nanoindenter setup. Compared with other techniques used in literature, a nanoindenter features the option to measure not only normal loads but also lateral forces and torques, both for sliding and rolling. Even though the interpretation/evaluation of the results still leaves various open questions, a big step was made towards understanding particle contacts and interactions and to directly obtain contact model parameters.

Normal force: Experimentally, the repulsive normal force between micron-sized borosilicate spheres and Si surfaces is well described by a Hertzian law, but the adhesion force decays with increasing surface roughness (on the scale of 0.3–3 nm). While the effect of the considerable surface roughness on the normal force is surprisingly small, it should lead to notable plastic deformations of the contacting micro-asperities.

Sliding, Rolling and Torsion: The influence of surface roughness and adhesion on pure sliding and pure rolling measurements was studied for the same particles on Si surfaces. In addition, novel rail experiments feature a combination of torsion and rolling motion. Due to the set-up, sliding and torsion occur only at the contact with the substrate; in contrast, rolling torques occur at both substrate and indenter contacts, i.e., the resulting rolling friction coefficient is an averaged quantity from the two contacts, which can involve different materials or surfaces. All motion types (pure sliding, pure rolling, mixed torsion and rolling) can be represented as relations between the measured lateral force and the applied normal load via an effective friction coefficient μ, and an effective adhesion, $f^{\nu} = \mu(f^{\mathrm{n}} + f_{\mathrm{a}}^{\nu})$, where ν stands for the motion type. The smallest normal forces typically display a mix of different motions, but the results are reliable for normal loads between 100 and 3000 μN.

All data can be fitted by either a linear or a non-linear model. The models assume independence between the adhesion and friction coefficients and the normal force. The former, linear model leads to constant friction factors for rolling and torsion (when scaled with the particle radius) that are much smaller than for sliding, but also to highly different predictions for the effective adhesion for the different motions, being highest for pure rolling. The latter, non-linear model takes into account the dependence of the rolling and torsion friction factors on the (predicted) contact radius by introducing it as a length scale into the yield criteria for the rolling and torsion torques. Unfortunately, the present set of data does not allow to decide which of the two models is the true one, so that both interpretations were presented in Ref. [11].

Sinter kinetics involve **temperature-, time- and size-dependent contact mechanisms** that result in an interesting sintering kinetics and mechanical properties during initial stage sintering. To indirectly calibrate the contact models, thin PS particle layers were investigated, utilising 3D tomography (FIB/SEM), nanoindentation and confocal microscopy. The experimental results indicate that the sinter kinetics and mechanical properties of particles with $r < 1\,\mu\text{m}$ are more caused by the contact deformation due to surface forces, whereas sintering of larger particles is characterised by viscous flow as the dominant mechanism. Consequently, larger particles require higher sintering temperatures and times to reach the same extent of sintering.

For a temperature- and pressure-dependent sintering model that includes the contribution of surface forces, we start from the elasto-plastic model of Luding [22, 23], and generalize it by introducing a rate of change for the permanent, plastic deformation at high temperatures. The contact model can simulate both contact sintering as well as compression, i.e., elastic repulsion, allowing the simulation of the free-flowing (cold) particles, their sintering, the cool-down and eventually the indentation tests in one single simulation framework (with one contact model, but parameters varying with pressure, temperature and time). Preliminary simulation results for either pure viscous or pure surface sintering (as based on theoretical predictions) respectively under- and over-predict the experimental results. A model taking into account both mechanisms (surface forces and viscous sintering), as well as the increase in particle radius due to sintering, may be able to fully explain the experimental observations.

Acknowledgements This work was carried out within the framework of the Key Research Program (SPP 1486 PiKo "Particles in Contact") grants LU 450/10, STA 1021/1 and KA 1724/1. The authors would like to thank the German Research Foundation (DFG) for their financial support during the SPP. The numerical simulations in this paper were carried out using the open-source code MercuryDPM [46, 53, 54], available via http://mercurydpm.org. This SPP and our research would not have been possible without Professor Tomas, who initiated the SPP, but sadly died and thus could not accompany us to the successful ending of the projects; we miss him and his inspirations about particles in contact very much. Special thanks also to Professor Antonyuk who led the SPP successfully to the end, as reflected by this book.

References

1. Besler, R., Rossetti da Silva, M., Rosario, J.J., Dosta, M., Heinrich, S., Janssen, R.: Sintering simulation of periodic macro porous alumina. J. Am. Ceram. Soc. **98**(11), 3496–3502 (2015)
2. Bierwisch, C., Polfer, P.: Scaling laws for implicit viscosities in smoothed particle hydrodynamics. In: EPJ Web of Conferences, vol. 140, p. 15008 (2017)
3. Breinlinger, T., Schubert, R., Hashibon, A., Kraft, T.: Modelling die filling for powders with complex rheology: a new DEM contact-model. In: Proceedings of 19th International Plansee Seminar. Plansee Group Service GmbH, Reutte, Austria (2017)
4. Brendel, L., Török, J., Kirsch, R., Bröckel, U.: A contact model for the yielding of caked granular materials. Granul. Matter **13**(6), 777–786 (2011)
5. de Gennes, P.G.: From rice to snow. In: Nishina Memorial Lectures. Volume 746 of Lecture Notes in Physics, pp. 297–318. Springer, Berlin/Heidelberg (2008)
6. Ding, W., Howard, A.J., Murthy Peri, M.D., Cetinkaya, C.: Rolling resistance moment of microspheres on surfaces: contact measurements. Philos. Mag., **87**(36), 5685–5696 (2007)
7. Fischer-Cripps, A.C.: A review of analysis methods for sub-micron indentation testing. Vacuum **58**(4), 569–585 (2000)
8. Freedonia: World Material Handling Products. Freedonia Group Inc. (2012)
9. Frenkel, J.A.: Viscous flow of crystalline bodies. J. Phys. **9**(5), 385–391 (1945)
10. Fuchs, R., Meyer, J., Staedler, T., Jiang, X.: Sliding and rolling of individual micrometre sized glass particles on rough silicon surfaces. Tribol. Mater. Surf. Interfaces **7**(2), 103–107 (2013)
11. Fuchs, R., Weinhart, T., Meyer, J., Zhuang, H., Staedler, T., Jiang, X., Luding, S.: Rolling, sliding and torsion of micron-sized silica particles: experimental, numerical and theoretical analysis. Granul. Matter **16**(3), 281–297 (2014)
12. Fuchs, R., Ye, M., Weinhart, T., Luding, S., Butt, H.-J., Kappl, M.: Sintering of polymer particle-experiments and modelling of temperature- and time-dependent contacts. In: Proceedings of the International Congress on Particle Technology, PARTEC (2016)
13. Fuchs, R., Weinhart, T., Ye, M., Luding, S., Butt, H.-J., Kappl, M.: Initial stage sintering of polymer particles. In: EPJ Web of Conferences, vol. 140, p. 13012. EDP Sciences (2017)
14. Harshe, Y.M., Lattuada, M.: Breakup of clusters in simple shear flow. J. Phys. Chem. B **120**(29), 7244–7252 (2008)
15. Hashibon, A.: A DEM model for history dependent powder flows. Comput. Part. Mech. **3**(4), 437 (2016)
16. Hertz, H.: Über die Berührung fester elastischer Körper. J. für die reine u. angew. Math. **92** (1882)
17. Imole, O.I., Kumar, N., Magnanimo, V., Luding, S.: Hydrostatic and shear behavior of frictionless granular assemblies under different deformation conditions. KONA Powder Part. J. **30**, 84–108 (2013)
18. Kuhn, M.R., Bagi, K.: Contact rolling and deformation in granular media. Int. J. Solids Struct. **41**(21), 5793–5820 (2004)
19. Laube, J., Drmann, M., Schmid, H.-J., Mdler, L., Colombi Ciacchi, L.: Dependencies of the adhesion forces between TiO_2 nanoparticles on size and ambient humidity. J. Phys. Chem. C **121**(28), 15294–15303 (2017)
20. Liu, D.L., Martin, J., Burnham, N.A.: Optimal roughness for minimal adhesion. Appl. Phys. Lett. **91**(4) (2007)
21. Luding, S.: Collisions & contacts between two particles. NATO ASI Ser. E Appl. Sci. Adv. Study Inst. **350**, 285–304 (1998)
22. Luding, S.: Cohesive, frictional powders: contact models for tension. Granul. Matter **10**(4), 235–246 (2008)
23. Luding, S., Manetsberger, K., Müllers, J.: A discrete model for long time sintering. J. Mech. Phys. Solids **53**(2), 455–491 (2005)
24. Mader-Arndt, K., Kutelova, Z., Fuchs, R., Meyer, J., Staedler, T., Hintz, W., Tomas, J.: Single particle contact versus particle packing behavior: model based analysis of chemically modified glass particles. Granul. Matter **16**(3), 359–375 (2014)

25. Marigo, M., Stitt, E.H.: DEM for industrial applications. KONA Powder Part. J. **32**, 236–252 (2015)
26. Mazur, S., Beckerbauer, R., Buckholz, J.: Particle size limits for sintering polymer colloids without viscous flow. Langmuir **13**(16), 4287–4294 (1997)
27. Mindlin, R.D.: Compliance of elastic bodies in contact. J. Appl. Mech. **16** (1949)
28. Mindlin, R.D., Deresiewicz, H.: Elastic spheres in contact under varying oblique forces. J. Appl. Mech. **20** (1953)
29. Nosewicz, S., Rojek, J., Pietrzak, K., Chmielewski, M.: Viscoelastic discrete element model of powder sintering. Powder Technol. **246**, 157–168 (2013)
30. Ormel, T., Magnanimo, V., Luding, S.: Modeling of asphalt and experiments with a discrete particles method. In: Conference Proceedings MAIREPAV7 2012 (2012)
31. Pasha, M., Dogbe, S., Hare, S., Hassanpour, A., Ghadiri, M.: A linear model of elasto-plastic and adhesive contact deformation. Granul. Matter **16**(1), 151–162 (2014)
32. Peri, M.D.M., Cetinkaya, C.: Adhesion characterization based on rolling resistance of individual microspheres on substrates: review of recent experimental progress. J. Adhes. Sci. Technol. **22**(5–6), 507–528 (2008)
33. Pokluda, O., Bellehumeur, C.T., Vlachopoulos, J.: Modification of Frenkel's model for sintering. AICHE J. **43**(12), 3253–3256 (1997)
34. Rojek, J., Labra, C., Su, O., Onate, E.: Comparative study of different discrete element models and evaluation of equivalent micromechanical parameters. Int. J. Solids Struct. **49**(13), 1497–1517 (2012)
35. Rojek, J., Nosewicz, S., Jurczak, K., Chmielewski, M., Bochenek, K., Pietrzak, K.: Discrete element simulation of powder compaction in cold uniaxial pressing with low pressure. Comput. Part. Mech. **3**(4), 513–524 (2016)
36. Roy, S., Luding, S., Weinhart, T.: Macroscopic bulk cohesion and torque for wet granular materials. In Conference for Conveying and Handling of Particulate Solids (2015)
37. Saito, S., Miyazaki, H.T., Sato, T., Takahashi, K.: Kinematics of mechanical and adhesional micromanipulation under a scanning electron microscope. J. Appl. Phys. **92**(9), 5140–5149 (2002)
38. Schilde, C., Burmeister, C.F., Kwade, A.: Measurement and simulation of micromechanical properties of nanostructured aggregates via nanoindentation and dem-simulation. Powder Technol. **259**, 1–13 (2014)
39. Singh, A., Magnanimo, V., Luding, S.: Mesoscale contact models for sticky particles. Powder Technol. (submitted)
40. Skorupski, K., Hellmers, J., Feng, W., Mroczka, J., Wriedt, T., Mädler, L.: Influence of sintering necks on the spectral behaviour of ITO clusters using the discrete dipole approximation. J. Quant. Spectrosc. Radiat. Transf. **159**, 11–18 (2015)
41. Steuben, J.C., Iliopoulos, A.P., Michopoulos, K.G.: Discrete element modeling of particle-based additive manufacturing processes. Comput. Methods **305**, 537–561 (2016)
42. Strege, S., Weuster, A., Zetzener, H., Kwade, A.: Approach to structural anisotropy in compacted cohesive powder. Granul. Matter **16**(3), 401–409 (2014)
43. Tabor, D.: Indentation hardness: Fifty years on—a personal view. Philos. Mag. A Phys. Condens. Matter Struct. Defects Mech. Prop. **74**(5), 1207–1212 (1996)
44. Thakur, S.C., Morrissey, J.P., Sun, J., Chen, J.F., Ooi, J.Y.: Micromechanical analysis of cohesive granular materials using the discrete element method with an adhesive elasto-plastic contact model. Granul. Matter **16**(3), 383–400 (2014)
45. Thakur, S.C., Ooi, J.Y., Ahmadian, H.: Scaling of discrete element model parameters for cohesionless and cohesive solids. Powder Technol. **293**, 130 (2016)
46. Thornton, A.R., Krijgsman, D.R., Fransen, R.H.A., Gonzalez Briones, S., Tunuguntla, D.R., te Voortwis, A., Luding, S., Bokhove, O., Weinhart, T.: Mercury-DPM: fast particle simulations in complex geometries. EnginSoft Newsl. Simul. Based Eng. Sci. **10**(1), 48–53 (2013)
47. Thornton, C., Cummins, S.J., Cleary, P.W.: An investigation of the comparative behaviour of alternative contact force models during inelastic collisions. Powder Technol. **233**, 30–46 (2013)

48. Tykhoniuk, R., Tomas, J., Luding, S., Kappl, M., Heim, L., Butt, H.-J.: Ultrafine cohesive powders: from interparticle contacts to continuum behaviour. Chem. Eng. Sci. **62**(11), 2843–2864 (2007)
49. van Zwol, P.J., Palasantzas, G., van de Schootbrugge, M., de Hosson, J.T.M., Craig, V.S.J.: Roughness of microspheres for force measurements. Langmuir **24**(14), 7528–7531 (2008)
50. Vastola, G., Zhang, G., Pei, Q.X., Zhang, Y.W.: Microstructure evolution during additive manufacturing. JOM **68**, 5 (2016)
51. Wahl, M., Brckel, U., Brendel, L., Feise, H.J., Weigl, B., Rck, M., Schwedes, J.: Understanding powder caking: predicting caking strength from individual particle contacts. Powder Technol. **188**(2), 147–152 (2008)
52. Walton, O.R., Braun, R.L.: Viscosity, granular temperature, and stress calculations for shearing assemblies of inelastic, frictional disks. J. Rheol. **30**(949) (1986)
53. Weinhart, T., et al.: MercuryDPM: fast, flexible particle simulations in complex geometries Part II: Applications. In: 5th International Conference on Particle-Based Methods—Fundamentals and Applications, PARTICLES 2017, pp. 123–134. International Center for Numerical Methods in Engineering (2017)
54. Weinhart, T., Tunuguntla, D.R., van Schrojenstein-Lantman, M.P., van Der Horn, A.J., Denissen, I.F.C., Windows-Yule, C.R., de Jong, A.C., Thornton, A.R.: MercuryDPM: a fast and flexible particle solver Part A: Technical advances. In: Springer Proceedings in Physics, vol. 188 (2017)
55. Zhang, L., DAcunzi, M., Kappl, M., Auernhammer, G.K., Vollmer, D., van Kats, C.M., van Blaaderen, A.: Hollow silica spheres: synthesis and mechanical properties. Langmuir, **25**(5), 2711–2717 (2009)
56. Zohdi, T.I.: Additive particle deposition and selective laser processing—a computational manufacturing framework. Comput. Mech. **54**(1), 171–191 (2014)